Electronic structure of β-Al_3Mg_2 and $Al_{13}Fe_4$ complex metallic alloys

Vipin Kumar Singh[1], Marian Krajčí[2], Shuvam Sarkar[1], Mohammad Balal[1], Sajal Barman[1], Pampa Sadhukhan[1], Andrei Gloskovskii[3], Michael Feuerbacher[4], Carsten Thomas[4], Philipp Ebert[4], Eli Rotenberg[5], Karsten Horn[6], Sudipta Roy Barman[1]
[1]*UGC-DAE Consortium for Scientific Research, Khandwa Road, Indore 452001, Madhya Pradesh, India*
[2]*Institute of Physics, Slovak Academy of Sciences, Dúbravská cesta 9, SK-84511 Bratislava, Slovak Republic*
[3]*Deutsches Elektronen-Synchrotron DESY, Notkestr. 85, D-22607 Hamburg, Germany*
[4]*Peter Grünberg Institut (PGI 5) and Ernst Ruska-Centrum für Mikroskopie und Spektroskopie mit Elektronen (ER-C 1), Forschungszentrum Jülich GmbH, D-52425 Jülich, Germany*
[5]*Advanced Light Source, E. O. Lawrence Berkeley National Laboratory, Berkeley, California 94720, USA and*
[6]*Fritz-Haber-Institut der Max-Planck-Gesellschaft, Faradayweg 4-6, 14195 Berlin, Germany*

We report a comparative study of the bulk electronic structure of two Al-based complex metallic alloys (CMAs), β-Al_3Mg_2 and $Al_{13}Fe_4$ using hard x-ray photoemission spectroscopy (HAXPES) interpreted on the basis of density functional theory (DFT) calculations. An experimental confirmation of the role of the Hume Rothery mechanism for the stability of the β-Al_3Mg_2 phase is established by identification of a shallow pseudogap near E_F from HAXPES and corroborated by DFT. An almost parabolic shape of the DOS, a large $n(E_F)$ and plasmon loss features that are similar to Al metal show its nearly free electron like nature. In the case of $Al_{13}Fe_4$ the total DOS exhibits a shallow pseudogap due to Al *s*- Fe *d* hybridization, which results in the DOS at E_F [$n(E_F)$] being large due to Fe *d* states. However, the Al *s* states show a deep pseudogap and this is revealed in HAXPES because of the large photoemission cross-section of the *s* states at high photon energies. The overall shape of the valence band is in excellent agreement with DFT for both the CMAs. The larger width of the Al core-level main peak and the plasmon loss peaks as well as the suppression of the intensities of the latter with respect to β-Al_3Mg_2 further underlines the importance of *sp*-*d* hybridization in $Al_{13}Fe_4$.

I. INTRODUCTION

Complex metallic alloys (CMAs) are a family of intermetallic compounds with complex structures characterized by the presence of large unit cells containing tens to thousands of atoms with well-defined atom clusters [1, 2]. The high structural complexity of CMAs, combined with two competing physical length scales, one dictated by unit-cell characteristics and the other by the cluster substructure, may have a considerable impact on their physical properties, electronic structures, and lattice dynamics [3]. CMAs have been suggested to be promising candidates for hydrogen-storage due to the presence of tetrahedral interstitial sites [5, 6]. β-Al_3Mg_2 with a unit cell of 1168 atoms is considered as one of the most complex intermetallic phase among the CMAs [4]. β-Al_3Mg_2 has many interesting mechanical properties useful for applications such as high strength-to-weight ratio and low frictional coefficient [7, 8]. In addition, Al-Mg alloys are corrosion resistant and highly weldable. β-Al_3Mg_2 is stable from its congruent melting point (451°C) down to low temperatures [9], and has been reported to exhibit superconductivity with T_c= 0.87 K [10, 11].

$Al_{13}Fe_4$ is another example of a CMA material that, unlike β-Al_3Mg_2, contains a 3*d* element and has a much smaller unit cell. Based on its local structure, it is considered to be a decagonal approximant [12], and the structure can be visualized as a four layer stacking along the [010] direction, with flat layers at y= 0 and 1/2 and two symmetrically equivalent puckered layers at y= 1/4 and 3/4. $Al_{13}Fe_4$ has recently drawn the interest of various research groups due to its remarkable chemical properties. It has been proposed to be a low cost environmentally benign catalyst for organic reactions [13–16]. $Al_{13}Fe_4$ also exhibits a significant anisotropy in its electronic and magnetic properties, the stacking direction being the most conducting direction for heat and electricity [17].

Turning to the electronic structure, the existence of a pseudogap across the Fermi level E_F in quasicrystals and their approximants has received considerable attention because of its role in stabilizing these phases [18, 19]. The approximants are CMAs with large unit cells and a local atomic arrangement identical to that of a quasicrystal. So attention has focused on the possible role of a pseudogap in stabilizing the structure of the CMAs [20]. Based on detailed first principle calculations, Mizutani *et al.* [20, 21] predicted that the stability of β-Al_3Mg_2 arises from the Hume-Rothery mechanism (its valence electron to atom (e/a) ratio being 2.6), implying the existence of a pseudogap at E_F. However, the authors could not calculate the DOS by density functional theory (DFT) because of its large unit cell. Degtyareva *et al.* also suggested Brillouin zone-Fermi sphere interaction as the cause of its stability [21]. An x-ray emission spectroscopy study reported a decrease in the intensity at E_F of the Mg 3p and Al 3p spectra of β-Al_3Mg_2 compared to that of pure Mg or Al, and this was presented as possible evidence of a pseudogap [22]. However, there was no evidence of the pseudogap from the spectral shape. Also, transport studies such as resistivity, specific heat, thermopower, as well as NMR Knight shift indicated metallic behavior and the absence of a pseudogap [6, 11]. The authors concluded that a pseudogap across E_F does not form due to the high structural complexity and intrinsic disorder of β-Al_3Mg_2. Thus, disagreement exists in the literature about the existence of a pseudogap in β-Al_3Mg_2. The electronic structure of $Al_{13}Fe_4$ calculated by DFT also showed a pseudogap at E_F that was related to hybridization of Al *s* and Fe *d* states [23]. Subsequent DFT calculations also confirmed the existence of the pseudogap [24, 25]. A recent DFT calculation by Fang *et al.* showed that the chemically stoichiometric composition of $Al_{13}Fe_4$ has the lowest energy of formation, it is non-magnetic and vacancies are unlikely to be present on either Al or Fe sites [26].

Although a low energy photoemission study has been reported for $Al_{13}Fe_4$ [27], there is no experimental study of the *bulk* electronic structure of either of the CMAs. Because of its sizeable probing depth, over the years hard x-ray photoemission spectroscopy (HAXPES) has emerged as the direct probe of the bulk electronic structure of materials [28–34]. In recent years, HAXPES has been used to study the bulk electronic structure of quasicrystalline and related materials. Among the important findings by HAXPES are the evidence of Anderson localization in *i*-Al-Pd-Re [35], heterogeneous valence states in Yb-based quasicrystalline approximants [36], and pseudogap around E_F in different icosahedral quasicrystals [19, 35, 37] and high-order approximants [38] have been reported. HAXPES uses photons in the range of 6-8 keV, and thus the inelastic mean free path of the photoelectrons increases to 6-10 nm [39]. Thus, surface effects, such as surface segregation in Al-Mg alloys [40] that could shroud the electronic structure, can be avoided in HAXPES. Here, we provide the first study of the bulk electronic structure of two important CMA materials *e.g.* β-Al_3Mg_2 and $Al_{13}Fe_4$ using HAXPES and DFT.

II. METHODS

The HAXPES measurements were performed at the P09 beamline [41] at PETRA III Deutsches Elektronen-Synchrotron, Hamburg, Germany. A post monochromator was used to improve the resolution and stability of the photon beam. All the measurements were performed using 5.94 keV unless otherwise stated, and some measurements were done with 7.92 keV photon energies (referred to as 6 and 8 keV henceforth). The photons were incident at a nearly grazing angle, and the measurements were carried out in the normal emission geometry in order to increase the bulk sensitivity, with the electron energy analyzer having an angular acceptance angle of ±15° [42]. The overall energy resolution (including source and the Phoibos 225 HV analyzer contribution) was 0.29 eV at 6 keV and 0.31 eV at 8 keV. The specimens were fractured *in-situ* at a base pressure of 1.5×10^{-8} mbar and were rapidly transferred to the main chamber at a base pressure of 1×10^{-10} mbar for measurements. The core-level spectra using low photon energy (0.24 keV) were measured at 7.0.1 beamline of the Advanced Light Source, U.S.A. on a *insitu* fractured β-Al_3Mg_2 specimen. **The x-ray photoelectron spectroscopy (XPS) data were recorded using Scientaomicron R4000 electron energy analyzer at a chamber base pressure of 9×10^{-11} mbar. For this purpose, the $Al_{13}Fe_4$(010) surface was prepared by repeated cycles of Ar ion sputtering and annealing up to 600°C for 90 min [27].** The single crystals were prepared by alloying the pure metal components several times under Argon in a levitation crucible. For β-Al_3Mg_2, the resulting alloy was cast into a rod-shaped mold 25 mm in diameter, used in a self flux growth to grow a single crystal. $Al_{13}Fe_4$ was grown using the Czochralski method and subsequently a large single crystal grain was extracted and used in the experiments.

The electronic structure calculations have been performed using the Vienna Ab initio Simulation Package (VASP) [43, 44]. The VASP performs an iterative solution of the Kohn–Sham equations of DFT within a plane wave basis. The PBE exchange correlation functional was employed [45, 46] and the basis set contained plane waves with a kinetic energy cutoff of 400 eV. The atomic structures of the models were optimized by static relaxation using a quasi-Newton method and with Hellmann-Feynman forces acting on the atoms. Both studied compounds Al_3Mg_2 and $Al_{13}Fe_4$ have complex atomic structures with many atoms in the elementary cells. The atomic structure of these compounds were analyzed, e.g. in Ref. 4 and 47.

For the calculation of their electronic density of states (DOS) the primitive cells from the alloy database [48] were used. As a part of the atomic sites in β-Al_3Mg_2 have undefined partial occupancy [4], the calculation was performed for the primitive cell of the closely related β'-Al_3Mg_2 phase, Pearson symbol *hR293*, space group $R3m$ (No. 160) , a= 19.969 Å, c= 48.911 Å [4]. The primitive cell of the β'-phase is almost the same as in the β-phase [49] and occupation of all atomic sites is well-defined. In the structural model of the β-phase [4, 48], the rhombohedral primitive cell of the β'-phase was used as the primitive cell to the cubic cell with composition of $Al_{724}Mg_{448}$, *i.e.* with 1172= 4×293 atoms ($cF1172$), which is very close to β-Al_3Mg_2 ($cF1168$). The chemical composition $Al_{61.775}Mg_{38.225}$ of the model is close to the reported composition $Al_{61.5}Mg_{38.5}$ of the β-phase [4]. The atomic sites in the primitive cell are occupied by 181 Al and 112 Mg atoms. The primitive cell of β'-Al_3Mg_2 is presented in Fig. S1 of the Supplementary Material (SM) [50]. The densities of states of this compound were calculated on the mesh of 4×4×4 k-points in the Brillouin zone.

Monoclinic $Al_{13}Fe_4$ belongs to the space group $C2/m$ (No. 12) (Pearson symbol *mC102*), a= 15.492 Å, b= 8.078 Å, c= 12.471 Å, β= 107.69° [51]. The DOS was calculated on a 5×9×6 k-point mesh. Local building blocks of $Al_{13}Fe_4$ are four-layer pentagonal bipyramids [27, 51]. The large scale structure can be also viewed as a planar tiling of hexagonal tiles [47]. The atomic sites in the unit cell are occupied by 78 Al and 24 Fe atoms (Fig. S2 [50]).

The valence band spectra have been calculated following our earlier work [33, 52] by multiplying the atom and angular momentum projected partial DOS (PDOS) by their respective photoemission cross-sections (σ) [53] and the Fermi function, which was then convoluted by a Gaussian function to take into account the instrumental resolution and an energy dependent Lorentzian function to take into account the lifetime broadening. The photoemission cross-section for Al $3d$ (Fe $4p$) that is not available in Ref. 53 is approximated to be equal to Fe $3d$ (Al $3p$). The core-level main peaks were fitted by using the Doniach-Šunjić (DS) lineshape [54], and asymmetric Lorentzian line shapes were used to represent the plasmon loss peaks [55]. The lifetime broadenings of the core level main peak, the DS asymmetry parameter (α), intensities, peak positions, and the inelastic background are varied independently, as in our earlier work [56].

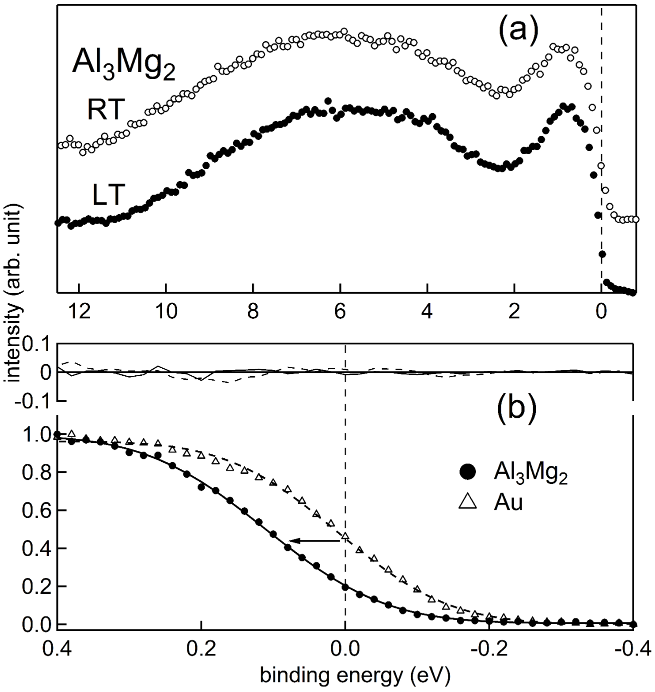

FIG. 1. (a) HAXPES valence band (VB) spectrum of β-Al_3Mg_2 recorded at 50 K (LT) and 300 K (RT) with 6 keV photon energy. The dashed black line shows position of the Fermi level (E_F). The RT spectrum is staggered along the vertical axis. (b) The near-E_F region of β-Al_3Mg_2 and Au at LT. The fitted curves (and residuals in the upper region) are shown by continuous and dashed lines for β-Al_3Mg_2 and Au, respectively.

III. RESULTS AND DISCUSSION

A. Electronic structure of β-Al_3Mg_2

The HAXPES valence band (VB) spectrum of β-Al_3Mg_2 in Fig. 1(a) shows a peak at 0.7 eV binding energy (BE). A broad hump centered around 6 eV is separated from the 0.7 eV peak by a valley centered at 2.3 eV. The spectrum taken at 300 K (RT) is similar to that at 50 K (LT). The near-E_F region recorded at LT with a smaller step size and better statistics shows a clear shift towards higher BE with respect to the Au Fermi edge, as shown by a horizontal arrow in Fig. 1(b). The Au foil was mounted adjacent to β-Al_3Mg_2 so that these are in electrical contact and at the same temperature. The unchanged position of the Au Fermi edge over the course of the measurement showed that there is no change in the photon energy that could explain this shift. To quantify the shift and examine the spectral shapes, we have performed a least square fitting using the Fermi function at the measurement temperature of 50 K, convoluted with a Gaussian function ($G(E)$, E is the BE) representing the instrumental resolution. The position of the Fermi edge, the full width at half maximum (FWHM) of $G(E)$, and the overall intensity were varied to arrive at the best fit. We find that both the β-Al_3Mg_2 and Au spectra are well described by the Fermi function, as shown by the fitted curves, as well as by the random scatter of the residual of the fit in Fig. 1(b). A shift of the β-Al_3Mg_2 Fermi edge towards higher BE with respect to Au is observed: the two spectra almost coincide if shifted by 95 meV, except for an extra broadening (FWHM= 0.31 eV) compared to Au (FWHM= 0.29 eV), as shown in Fig. S3 [50].

The above mentioned shift observed in β-Al_3Mg_2 is unlikely to be related to the opening up of a band gap or pseudogap since the Fermi function describes its shape well; rather it is likely to be related to the recoil effect that is generally observed in the HAXPES spectra of low mass materials [57–62]. In the photoemission process, when a photoelectron of mass m is emitted with a large kinetic energy (E_{kin}) and momentum (k_f) from an atom of mass M, the photoelectron delivers a recoil energy (E_R) to that atom, which is given by $E_R \approx (\frac{m}{M}) \times E_{kin}$ [57]. The photoelectrons lose this energy E_R resulting in a recoil shift towards higher BE. It is interesting to note that this effect has also been observed for the Fermi edge of light metals such as Al (atomic mass 27 amu) compared to heavier Au (197 amu) [60]. Takata *et al.* reported a 120 meV shift as well as a broadening of the Al metal Fermi edge with respect to Au using $h\nu$= 8 keV [60]. Since Mg (24.3 amu) is lighter than Al, in β-Al_3Mg_2 the recoil shift of the Fermi edge is expected. The broadening of the Fermi edge in β-Al_3Mg_2 compared to Au (Fig. S3) is also a signature of this effect. The 95 meV shift observed here is somewhat smaller than for Al because a lower photon energy (6 keV) was used, since the $E_R \propto E_{kin}$. The occurrence of a recoil effect in the valence band electrons that are delocalized has been attributed to the coupling of the electrons with the crystal lattice, and that their wave functions follow the atomic motion adiabatically [60].

Thus, unlike high-order approximants [38] or quasicrystals [19, 37, 63], the near-E_F HAXPES spectrum of β-Al_3Mg_2 shows a well developed metallic Fermi edge. This is consistent with its metallic resistivity (33.2 $\mu\Omega$ cm at 4 K [6]) with a positive temperature coefficient, showing the dominance of electron-phonon interactions as in a metal [6]. On the other hand, a Hume Rothery mechanism induced pseudogap, albeit shallow, has been predicted theoretically [2]. A reason why it could not be identified from transport and NMR studies was assigned to disorder in the specimen [6, 11]. To investigate the existence of a pseudogap in an ordered structure and explain the characteristic shape of the valence band, we have performed DFT calculations for $\beta' Al_3Mg_2$ (Fig. S1 [50]).

The total density of states (DOS) in Fig. 2(a) has a parabolic shape, as shown by a fitting over the whole range with a parabola indicating its nearly free electron-like nature (dashed red line given by $a \times \sqrt{E-b}$). From the fitting, we obtain a= 0.13 and the band minimum b = 10 eV. The unoccupied DOS is rather featureless, dominated by the p states. However, there are some notable deviations from the parabolic shape: for example, a small suppression of states at E_F is observed, which is highlighted by a red oval in Fig. 2(a). The suppression of states at E_F with respect to the free electron parabola is a signature of a shallow pseudogap and we are able to identify this in our HAXPES VB spectrum also (as discussed later). A larger dip of 12% with a width of 1 eV is observed around 1.5 eV in the total DOS. On the higher BE side, the total DOS

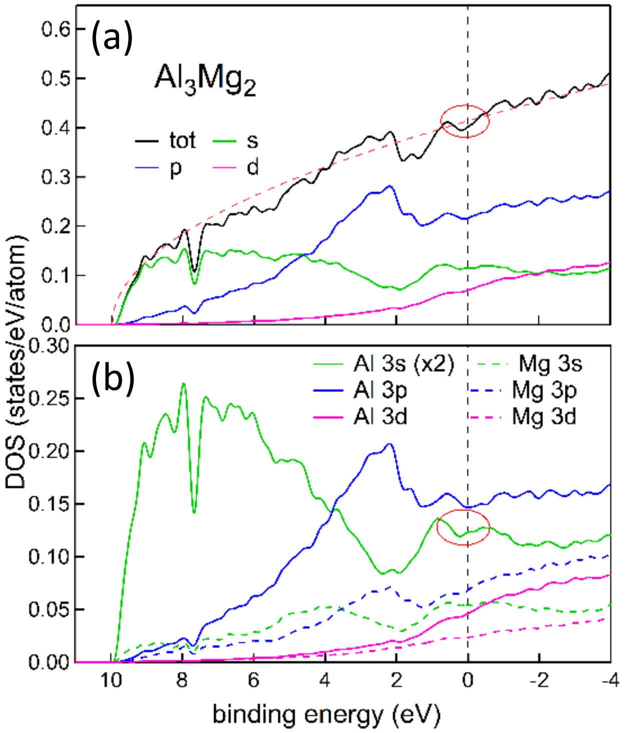

FIG. 2. (a) The total density of states (DOS) and (b) the atom and angular momentum projected partial DOS (PDOS) of β-Al_3Mg_2.

has a sharp slope, caused by the Al and Mg *p* states that are pushed down to peak at 2.4 eV. The lower BE side has a gentler slope caused by the dip observed in the Al and Mg *s* states at 2.2 eV. The dip at 1.5 eV as well as a prominent dip at 7.5 eV [Fig. 2(a,b)] might also arise due to interference of electrons with the lattice planes, as was observed for γ-$Mg_{17}Al_{12}$ where a real gap results at 7.2 eV BE [20].

The calculated VB shown in Fig. 3 has a different shape compared to the DOS, clearly caused by the difference in the photoemission cross-sections of each contributing electronic levels. It is in excellent agreement with experiment: the peak-valley-hump structure is clearly visible at similar energies. The partial contributions show that the *s* states dominate, while the *p* states are weak. The hump arises mainly from Al 3*s* states peaking around 6.5 eV, with some contribution from the Mg 3*s* states around 4 eV resulting in its slightly asymmetric shape towards lower BE. The valley around 2 eV can be related to the dip in the DOS at the same energy for the Al and Mg *s* states. The shallow pseudogap at E_F discussed above for total DOS [Fig. 2(a)] is prominently observed in the Al *s* and *p* states [highlighted by a red oval in Fig. 2(b) for the former]. This is manifested in the calculated partial contribution to the VB as a decreasing DOS starting from the peak at 0.7 eV [red down arrow in Fig. 3] to the inflection point at 0.3 eV [red tick]. The latter appears due to the presence of the Fermi edge. The decreasing DOS also has its signature in the HAXPES, as observable both in the wide and the near-E_F spectrum [black filled and green open circles, respectively in Fig. 3], where the maximum is shown by a black down arrow and the inflection point by a black tick. The suppression can be estimated to be ∼10%. Thus, the presence of a shallow pseudogap is established from experiment and also corroborated by DFT. This shows that the stability of β-Al_3Mg_2 is related to the Hume Rothery mechanism that was predicted earlier by Mizutani *et al.*, where 84 Brillouin zone planes interact almost simultaneously with a more or less spherical Fermi surface [2].

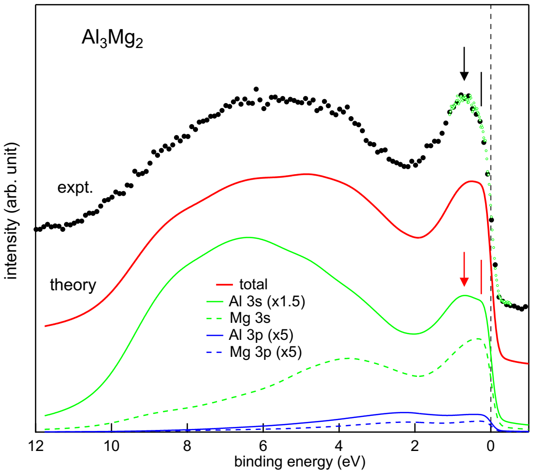

FIG. 3. The calculated VB (red curve) of β-Al_3Mg_2 along with the partial contributions compared with the HAXPES VB spectrum (black filled circles) taken at LT. The spectra are staggered along the vertical axis for clarity of presentation. The near-E_F region of the HAXPES VB spectrum (green open circles) recorded with smaller step size at LT is overlaid on the wide range VB spectrum. The experimental VB spectra are shifted by the 95 meV towards E_F to compensate for the recoil effect that is not considered in the calculation.

B. Electronic structure of $Al_{13}Fe_4$

The VB of $Al_{13}Fe_4$ shows a broad hump centered around 6 eV with a FWHM of about 7 eV [Fig. 4(a)]. A weak dip at about 2.7 eV is observed, as shown by a down arrow. The near-E_F region in inset shows a weak hump around 0.6 eV (up arrow), which is visible for both the 6 and 8 keV spectra. In Fig. 4(b), a comparison with the Au Fermi edge recorded under similar conditions shows that the $Al_{13}Fe_4$ near-E_F spectral shape is rather suppressed. The Au Fermi edge is fitted nicely by the Fermi function convoluted with $G(E)$. A similar least square fitting for $Al_{13}Fe_4$ keeping $G(E)$ and the position of the Fermi edge fixed fails completely, as shown by the large deviations in Fig. 4(b). In fact, an indication of a pseudogap in $Al_{13}Fe_4$ is obtained from the large negative residual around E_F shown in the upper region of panel (b). In Fig. 4(c), to establish the presence of the pseudogap, we perform a least square curve fitting assuming an analytic shape of the pseudogap: an inverted Lorentzian function, multiplied by a free electron parabola

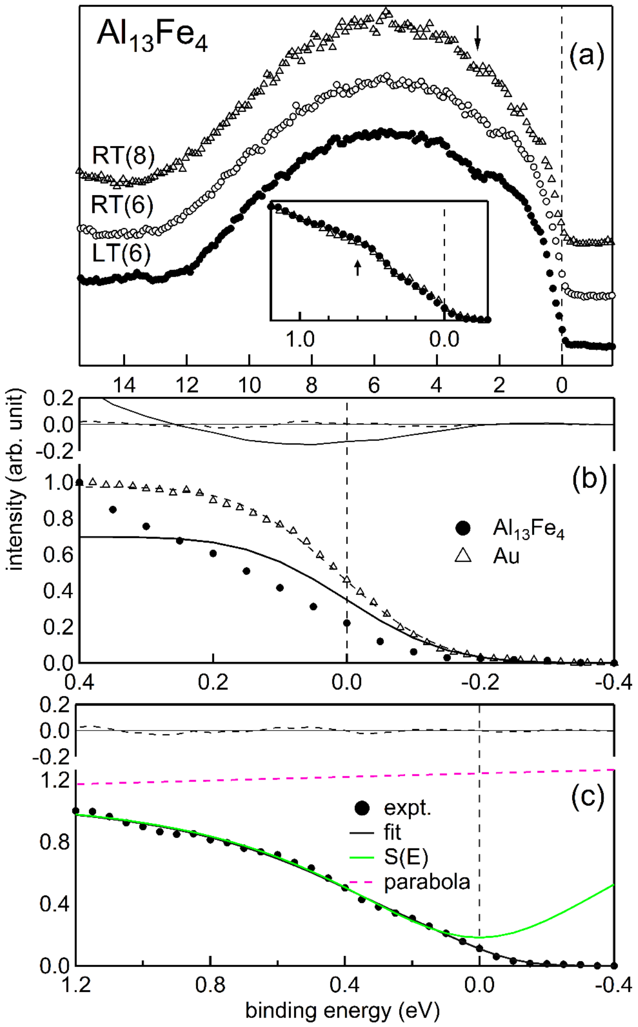

FIG. 4. (a) HAXPES VB spectrum of $Al_{13}Fe_4$ taken at RT and LT, the photon energy in keV is given within the brackets. Inset shows the near-E_F region. (b) The near-E_F region of $Al_{13}Fe_4$ and Au at LT. The fitted curves (and residuals in the upper region) are shown by continuous and dashed lines for $Al_{13}Fe_4$ and Au, respectively. (c) The near E_F region of $Al_{13}Fe_4$ fitted using $S(E)$ (green curve), which is given by an inverted Lorentzian function multiplied by a free electron parabola (Equation 1). The residual (black dashed curve) is shown in the upper region.

$[a' \sqrt{(E-b')}]$. Such an approach has been used earlier for related systems such as high order approximants [38] and quasicrystals [19, 35, 37, 65]. The expression used for fitting is given by $[I \times S(E) \times f(E,T)] \otimes G(E)$ where

$$S(E) = [a' \times \sqrt{(E-b')}] \times [1 - \frac{C_L \Gamma_L^2}{E^2 + \Gamma_L^2}] \qquad (1)$$

represents the pseudogap defined as a minimum in the density of states with respect to a free electron parabola. $[1 - \frac{C_L \Gamma_L^2}{E^2 + \Gamma_L^2}]$ represents the inverted Lorentzian function where C_L indicates the depth of the pseudogap and $2\Gamma_L$ is the FWHM. For C_L= 1, the pseudogap is fully formed with zero spectral intensity at E= 0. On the other hand, for C_L= 0, the pseudogap is absent and $S(E)$ is represented by the parabola [38]. $f(E,T)$ is the Fermi function at temperature T and I is a multiplicative factor. While all the other parameters are varied during the curve fitting, b' and the position of the minimum of $S(E)$ are kept fixed at the band minimum and E_F, respectively. The band minimum (= 10.9 eV) is obtained from the total DOS of $Al_{13}Fe_4$ calculated by DFT in Fig. 5(a). **In order to examine whether the near-E_F spectrum shifts towards larger BE due to recoil effect in the VB, the position of E_F is allowed to vary. However, its converged position remains essentially unchanged. If $G(E)$ is also allowed to vary, the broadening does not exceed the instrumental resolution. These two observations indicate that the recoil effect of the VB is not significant in $Al_{13}Fe_4$. This is also supported by the inset of Fig. 4(a) where the 6 and 8 keV near-E_F spectra almost coincide with each other. If recoil effect is present, a detectable shift could be expected between 6 and 8 keV, as reported for Al metal E_F [19, 64] and also C 1s core-level spectrum of graphite [58]. Possible reason for negligible recoil shift observed in the VB of $Al_{13}Fe_4$ and whether it is visible in the core-level spectra are discussed latter in section III.C.** We find that the quality of the fitting in Fig. 4(c) is good, as shown by the residual (black dashed curve). The existence of the pseudogap is established by the shape of $S(E)$ obtained from the fitting [green curve in Fig. 4(c)] that shows a well formed minimum with the C_L value being 0.8.

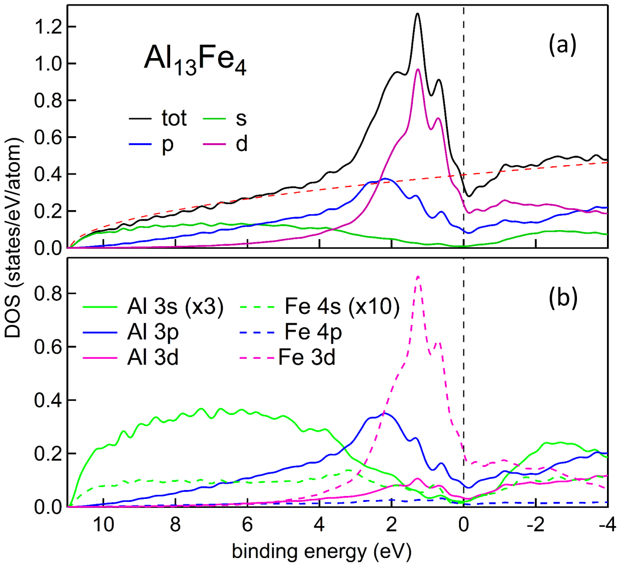

FIG. 5. (a) The calculated total DOS and (b) the atom and angular momentum specific PDOS of $Al_{13}Fe_4$.

In order to explain the shape of the VB and the origin of the pseudogap, we have performed DFT calculations for the mC102 structure of $Al_{13}Fe_4$ [47, 48]. The unit cell consists of 102 atoms with 78 Al atoms in 15 inequivalent sites and 24 Fe atoms in 5 inequivalent sites [Fig. S2 of SM [50]]. The most intense peak in the total DOS of $Al_{13}Fe_4$ is at 1.3 eV,

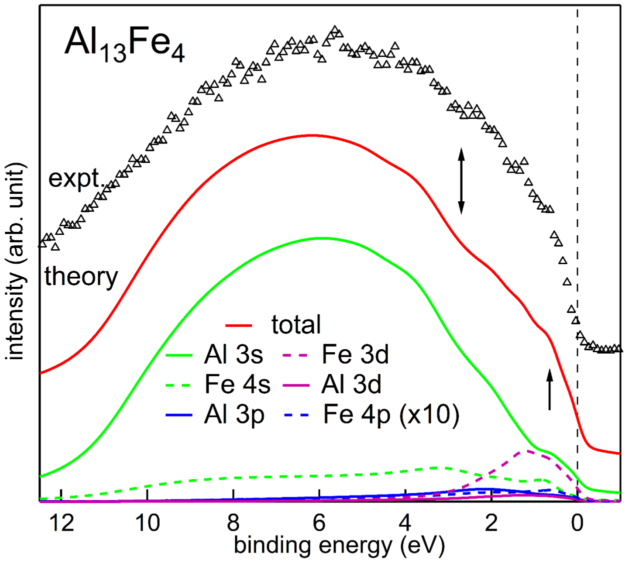

FIG. 6. The calculated VB (red curve) and the partial contributions of $Al_{13}Fe_4$ compared with the experimental VB spectra at LT with 8 keV (black open triangle) shown staggered along the vertical axis.

with two lesser intensity peaks on its sides at 1.9 and 0.7 eV [Fig. 5(a)]. The PDOS in Fig. 5(b) shows that the peaks at 1.3 and 0.7 eV arise primarily from Fe 3d states; however both Al 3p and 3s have peaks at the same position, although of lesser intensity. The peak at 1.9 eV arises from a peak in the Al p PDOS, but shoulders of Fe d as well as Al s states contribute. The appearance of peaks at a similar BE between Al sp and Fe d states suggests the importance of sp-d hybridization in $Al_{13}Fe_4$. A parabola represented by $a\times\sqrt{E-b}$, where a= 0.12 and b= 10.9 eV obtained by fitting is superimposed on the DOS as a dashed red curve. It shows that from the band minimum at 10.9 eV to about 5 eV, the DOS has a parabolic shape, and deviates beyond that due to the Fe d states. However, in the unoccupied region above -1.5 eV, the DOS continues to be nearly free electron like. It is interesting to note that a suppression from the parabolic DOS around E_F is clearly observed with the minimum at -0.15 eV. This suppression is related to the pseudogap showing with a decrease in DOS of about 30% with respect to the free electron parabola. However, the pseudogap seems to be less pronounced compared to the experiment [Fig. 4(c)]. Also, $n(E_F)$ (= 0.34 states/eV/atom) is quite large, which is primarily due to Fe d states, as shown by $n_{Fe3d}(E_F)$= 0.2 states/eV/atom. In contrast, the Al s states show a symmetric deep minimum around E_F with very small $n_{Al3s}(E_F)$ (= 0.01 states/eV/atom). The contribution of Fe 4s states is small near E_F, but it also shows a minimum with n_{Fe4s} almost zero. Thus, it is the PDOS of the s states that show a deep nearly symmetric pseudogap around E_F, in contrast to the Fe d states. This indicates a more covalent character of the Al s- Fe s bonding, and we have seen earlier that covalent Al-TM bonds can create a deep pseudogap or even a semiconducting gap [35].

Although the Fe d peak is most intense in the DOS, it is not observed in the HAXPES VB in Fig. 4(a). We calculated the VB in Fig. 6 and it shows excellent agreement with experiment: the broad hump at 6 eV with similar FWHM and the dip around 2.7 eV (double arrow), both entirely related to Al s states, are evident in the calculated VB. Morever, the weak hump at 0.6 eV (up arrow) related to Al s and Fe d states is also observed. The Fe d peak is not observed because of its lower photoemission cross-section (σ) compared to the Al s states; for example, at 8 keV, $\sigma_{Fe3d}/\sigma_{Al3s}$ is 0.03, whereas for 21.2 eV [He I ultra-violet photoemission spectroscopy (UPS)] it increases to 4.72 [53]. Similarly, $\sigma_{Fe3d}/\sigma_{Fe4s}$ is 0.026 at 8 keV, whereas it increases to 11.9 for UPS [53]. Thus, the overall shape of the VB is so different from the DOS because of the much larger cross-section of the s states in the hard x-ray regime. The s states have larger cross-section because of the increased oscillation in their radial wave function that leads to a larger overlap with the strongly oscillatory photoelectron wave function [57]. Thus, despite a much larger PDOS, in the near-E_F region largest contribution is from Al s, followed by Fe d and Fe s. The contribution of Fe s states is also enhanced substantially such that it is the second dominant contribution in the 2 to 12 eV range. *The predominance of the s states in HAXPES explains the occurrence of prominent pseudogap in Fig. 4(a), and there is no contradiction with a less prominent pseudogap observed in total DOS in Fig. 5(a).* This also shows that due to the larger cross-section of the Fe 3d states at low photon energies the pseudogap was not observed (rather a prominent Fe 3d related peak around 1 eV was observed) in a previous UPS measurement [27]. A prominent pseudogap in HAXPES would normally imply that the resistivity would be larger than in normal metals, as observed in quasicrystals [38]. However, Dolinšek and Smontara [66] showed a metallic resistivity for $Al_{13}Fe_4$ with large positive temperature coefficient, the resistivity varied between 2.5-14 $\mu\Omega$cm [66] at 2 K depending on the crystallographic direction. This metallic resistivity behavior of $Al_{13}Fe_4$ could be explained by its dependence on $n(E_F)$ that is large due to the Fe d states.

C. Core-level spectra of β-Al_3Mg_2 and $Al_{13}Fe_4$

Turning to the core-level spectra, the Al 2s signal of β-Al_3Mg_2 and $Al_{13}Fe_4$ in Fig. 7(a) show multiple bulk plasmon ($n\omega_p$, n= 1-3) loss peaks as in Al metal [67]. However, while the first plasmon loss peak ($1\omega_p$) for Al appears at 15.4 eV, for β-Al_3Mg_2 it is smaller (13.5 eV), whereas for $Al_{13}Fe_4$ it is larger (17.4 eV). Since the plasmon energy is proportional to the square root of the free electron density n_e (ω_p^2= $4\pi n_e e^2/m$), the larger electron density in $Al_{13}Fe_4$ due to additional d electrons (Fe shell configuration being $3d^64s^2$) compared to Al ($3s^23p^1$) increases its energy. On the other hand, Mg has one electron less in the outer shell $3s^2$ compared to Al resulting in a lower electron density and plasmon energy in β-Al_3Mg_2.

The other interesting observation is that the relative intensity and the FWHM of the bulk plasmons of β-Al_3Mg_2 are nearly similar to Al. For example, from the fitting, the relative intensity of $1\omega_p$ ($2\omega_p$) with respect to the main peak for Al metal is 0.64 (0.26), whereas for β-Al_3Mg_2 it is 0.54 (0.23)

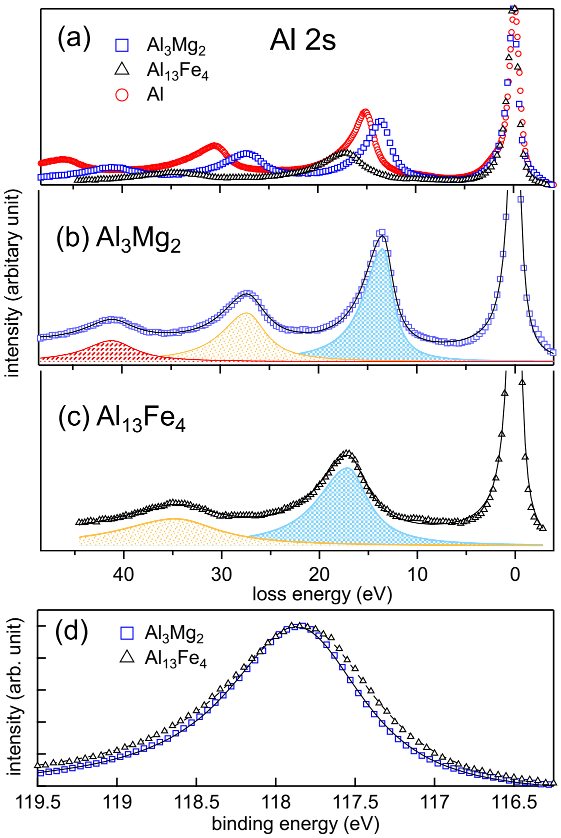

FIG. 7. (a) Al 2s HAXPES core-level spectra showing the plasmon loss region for β-Al$_3$Mg$_2$, Al$_{13}$Fe$_4$ and Al metal **taken with 6 keV**. The spectra are normalized to the same intensity at the main peak that is aligned to zero in the energy loss scale. The least square fitting (black curve) of the plasmon loss region of (b) β-Al$_3$Mg$_2$ and (c) Al$_{13}$Fe$_4$. The $1\omega_p$, $2\omega_p$, and $3\omega_p$ plasmon peaks are shaded by cyan, yellow and red colors, respectively. (d) The Al 2s main peak of β-Al$_3$Mg$_2$ and Al$_{13}$Fe$_4$ along with the fitted solid and dashed curves, respectively.

[Fig. 7(b)]. The FWHM of $1\omega_p$ ($2\omega_p$) for Al metal is 3.1 (4.2) eV, whereas for β-Al$_3$Mg$_2$ it is 3.6 (5.5) eV. This shows that the plasmons are of similar nature between Al and β-Al$_3$Mg$_2$, indicating the nearly free electron nature of the latter. In contrast, for Al$_{13}$Fe$_4$ the relative intensity decreases to 0.3 (0.1), while the FWHM increases to 6.3 (12.1) eV for $1\omega_p$ ($2\omega_p$) [Fig. 7(c)]. This can be related to the $sp-d$ hybridization process due to which the sp electron-related plasmon excitation is damped by the d electron interband transitions [68–72].

A further interesting difference between β-Al$_3$Mg$_2$ and Al$_{13}$Fe$_4$ is the larger width of the Al 2s main peak in the latter [Fig. 7(d)]. From the fitting, we find the intrinsic lifetime widths (γ) of β-Al$_3$Mg$_2$ to be 0.45 eV, similar to that of Al metal (γ= 0.42 [38]). On the other hand, for Al$_{13}$Fe$_4$ γ is considerably larger (0.52 eV). A larger width implies a decreasing final state-life time in the latter, which could be associated with Al sp- Fe d hybridization [38]. This is also facilitated by relatively smaller Al-Fe distances, *i.e.*, the nearest neighbour distance being 2.345Å [73, 74]. Thus, the changes in the plasmon line shape as well as that of the Al 2s main peak indicates the important role played by Al sp- Fe d hybridization in Al$_{13}$Fe$_4$.

The recoil effect in the VB of β-Al$_3$Mg$_2$ shown in Fig. 1(b) indicates that it might also be visible in the core-level spectrum. So, in Fig. S4 [50], we compared the Al 2p HAXPES spectrum with that measured using a lower photon energy (0.24 keV). The BE scales are calibrated accurately (<10 meV) from the position of the Fermi edge that was measured around the same time as the core-level peaks. The 2$p_{3/2}$ and 2$p_{1/2}$ components are separately visible in the better resolution 0.24 keV spectrum, showing a spin-orbit splitting of 0.4 eV. A fitting of the 6 keV spectrum using least square error minimization method with two DS line shapes representing 2$p_{3/2}$ (blue curve) and 2$p_{1/2}$ (red curve) is performed by fixing the spin-orbit splitting at 0.4 eV, and the life-time broadening and DS asymmetry parameter are kept equal for both the components. A recoil shift of E_R∼0.1 eV is obtained, as indicated by the horizontal arrows in Fig. S4.

In Fig. S5, the Al 2s HAXPES (6 and 8 keV) core-level spectra of Al$_{13}$Fe$_4$ are compared with the lower photon energy XPS spectrum taken with monochromatic AlKα radiation (1.48 keV). The curve fitting is performed using a single DS component for all the three spectra. The scatter in the data is less and the quality of the fitting is good such that it is possible to identify a small but finite E_R of ≈0.05 eV, as shown by a horizontal arrow in Fig. S5. Substantially reduced E_R compared to β-Al$_3$Mg$_2$ is possibly related to the larger mass of Fe (55.8 u) compared to Mg (24.3 u). Note that in Al$_{13}$Fe$_4$, in comparison to a finite E_R for the core-level, negligible recoil effect is observed in the VB (discussed earlier in section III.B). This shows that the recoil effect in the VB that involves extended Bloch wave functions is a complex phenomenon possibly related to the detailed nature of the Bloch states and the phonon modes. In this case, the strong hybridization of the Al sp and Fe d states near E_F might play an important role. This proposition is supported by an earlier study where negligible recoil effect in VO$_2$ in contrast to LiV$_2$O$_4$ was related to a smaller V-O bond length in the former [61].

IV. CONCLUSIONS

We present a comparative study of the electronic structures of two Al-based complex metallic alloys β-Al$_3$Mg$_2$ and Al$_{13}$Fe$_4$. From the shape of the valence band in the near-E_F region, we identify a shallow pseudogap in β-Al$_3$Mg$_2$ from HAXPES that is supported by our DFT calculations. The stability of the complex structure of β-Al$_3$Mg$_2$ is thus established to be due to the Hume Rothery mechanism. From the nearly parabolic shape of the DOS, a large $n(E_F)$ and the plasmon loss features (similar to Al metal), we conclude that β-Al$_3$Mg$_2$ is a nearly free electron metal. A recoil effect in the valence band **(also in the core-level spectrum)** is observed for β-Al$_3$Mg$_2$ that is of similar magnitude to that reported for

Al metal. The analysis of our data shows that Al *sp*- Fe *d* hybridization plays an important role in the electronic structure of $Al_{13}Fe_4$. A pronounced pseudogap is observed in HAXPES since the spectrum is dominated by the *s* states due to its larger photoemission cross-section, in agreement with DFT. However, the total DOS exhibits a shallow pseudogap with large $n(E_F)$ due to Fe *d* states that is responsible for its metallic behavior. The larger width of the Al core level main peak and the plasmon loss peaks, as well as the suppression of the latter compared to Al metal shows the importance of *sp-d* hybridization in $Al_{13}Fe_4$. Our work demonstrates the power of HAXPES and DFT in investigating the intriguing electronic structure of the complex metallic alloys and sheds light on their stabilization mechanisms.

Acknowledgment. The HAXPES experiments were carried out at PETRA III of Deutsches Elektronen-Synchrotron, a member of Helmholtz-Gemeinschaft Deutscher Forschungszentren. Financial support by the D.S.T., Government of India within the framework of India@DESY collaboration is gratefully acknowledged. C. Schlueter, W. Drube, C. Narayana and M. Sanyal are thanked for support and encouragement. M.K. would like to thank the Slovak Grant Agency VEGA (grant no. 2/0144/21) and APVV (grant nos. 19-0369 and 20-0124) for support. This research used resources of the Advanced Light Source, which is a DOE Office of Science User Facility under contract no. DE-AC02-05CH11231.

---

[1] K. Urban and M. Feuerbacher, Non-Cryst. Solids **143**, 334 (2004).

[2] U. Mizutani, Hume-Rothery Rules for Structurally Complex Alloy Phases (CRC Press, Boca Raton, FL, 2010), pp. 121-138.

[3] E. Macia, Aperiodic Structures in Condensed Matter:Fundamentals and Applications (Taylor and Francis, London, 2009).

[4] M. Feuerbacher *et al.* Z. Kristallogr. **222**, 259 (2007).

[5] F. C. Frank and J. S. Kasper, Acta Cryst. **12**, 483 (1959).

[6] J. Dolinsěk, T. Apih, P. Jeglič, I. Smiljanić, A. Bilušić, Ž. Bihar, A. Smontara, Z. Jagličić, M. Heggen, and M. Feuerbacher, Intermetallics **15**, 1367 (2007).

[7] H. Ramezanalizadeh, M. Emamy, and M. Shokouhimehr, Tribol. Trans. **59**, 219 (2016).

[8] S. Scudino, G. Liu, M. Sakaliyska, K.B. Surreddi, and J. Eckert, Acta Mater. **57**, 4529 (2009).

[9] J. L. Murray, Bull. Alloy. Phase Diagr. **60**, (1982).

[10] E. Bauer, H. Kaldarar, R. Lackner, H. Michor, W. Steiner, E.-W. Scheidt, A. Galatanu, F. Marabelli, T. Wazumi, K. Kumagai, and M. Feuerbacher, Phys. Rev. B **76**, 014528 (2007).

[11] S. Vrtnik, S. Jazbec, M. Jagodič, A. Korelec, L. Hosnar, Z Jagličić, P. Jeglič, M. Feuerbacher, U. Mizutani, and J. Dolinsěk, J. Phys.: Condens. Matter. **25**, 425703 (14pp) (2013).

[12] A. I. Goldman and K. F. Kelton, Rev. Mod. Phys. **65**, 213 (1993).

[13] M. Armbrüster, K. Kovnir, M. Friedrich, D. Teschner, G. Wowsnick, M. Hahne, P. Gille, L. Szentmiklósi, M. Feuerbacher, M. Heggen, F. Girgsdies, D. Rosenthal, R. Schlögl, and Yu. Grin, Nat. Mat. **11**, 690 (2010).

[14] I. G. Aviziotis, T. Duguet, K. Soussi, M. Heggen, M. Lafont, F. Morfin, S. Mishra, S. Daniele, A. G. Boudouvis, and C. Vahlas, Phys. Status Solidi A **215**, 1700692 (2018).

[15] L. Piccolo, C. Chatelier, M.-C. De Weerd, F. Morfin, J. Ledieu, V. Fournèe, P. Gille, and E. Gaudry, Sci. Technol. Adv. Mater. **20**, 557 (2019).

[16] A. Zięba, K. Stan-Głowińska, P. Czaja, Ł. Rogal, J. Przewoźnik, D. Duraczyńska, E. M. Serwicka, and L. Lityńska-Dobrzyńska, Microsc. Microanal. 1 (2021).

[17] P. Popcevic, A. Smontara, J. Ivkov, M. Wencka, M. Komelj, P. Jeglic, S. Vrtnik, M. Bobnar, Z. Jaglicic, B. Bauer, P. Gille, H. Borrmann, U. Burkhardt, Yu. Grin, and J. Dolinsěk, Phys. Rev. B **81**, 184203 (2010).

[18] J. Hafner and M. Krajčí, Phys. Rev. Lett. **68**, 2321 (1992).

[19] J. Nayak, M. Maniraj, A. Rai, S. Singh, P. Rajput, A. Gloskovskii, J. Zegenhagen, D. L. Schlagel, T. A. Lograsso, K. Horn, and S. R. Barman, Phys. Rev. Lett. **109**, 216403 (2012).

[20] U. Mizutani, Y. Kondo, Y. Nishino, M. Inukai, M. Feuerbacher, and H. Sato, J. Phys.: Condens. Matter. **22**, 485501 (2010).

[21] V. F. Degtyareva and N. S. Afonikova, Crystals **7**, 359 (2017).

[22] V. Fournèe, E. Belin-Ferree, A. Sadoc, P. Donnadieu, A. M. Flank, and H. Muller, J. Phys.: Condens. Matter. **11**, 191 (1999).

[23] T. Fujiwara and T. Yokokawa, Phys. Rev. Lett. **63**, 333 (1991).

[24] M. A. Albedah, F. Nejadsattari, Z. M. Stadnik, and J. Przewoźnik, J. Alloys Compd. **619**, 839 (2015).

[25] I. Ullah, S. Mehmood, Z. Ali, G. Rehman, I. Khan, and I. Ahmad, Int. J. Mod. Phys. B **32**, 1850201 (2018).

[26] C. M. Fang, A. Dinsdale, Z. P. Que, and Z. Fan, J. Phys.: Mater. **2**, 015004 (2019).

[27] J. Ledieu, E. Gaudry, L. N. S. Loli, S. A. Villaseca, M.-C. de Weerd, M. Hahne, P. Gille, Y. Grin, J.-M. Dubois, and V. Fournèe, Phys. Rev. Lett. **110**, 076102 (2013).

[28] K. Kobayashi, M. Yabashi, Y. Takata, T. Tokushima, S. Shin, K. Tamasaku, D. Miwa, and T. Ishikawa, H. Nohira and T. Hattori, Y. Sugita, O. Nakatsuka, A. Sakai, and S. Zaima, Appl. Phys. Lett. **83**, 1005 (2003).

[29] A. X. Gray, J. Minár, S. Ueda, P. R. Stone, Y. Yamashita, J. Fujii, J. Braun, L. Plucinski, C. M. Schneider, G. Panaccione, H. Ebert, O. D. Dubon, K. Kobayashi, and C. S. Fadley, Nat. Mater. **11**, 957 (2012); *ibid* Nat. Mater. **10**, 759 (2011).

[30] T. Ohtsuki, A. Chainani, R. Eguchi, M. Matsunami, Y. Takata, M. Taguchi, Y. Nishino, K. Tamasaku, M. Yabashi, T. Ishikawa, M. Oura, Y. Senba, H. Ohashi, and S. Shin, Phys. Rev. Lett. **106**, 047602 (2011).

[31] M. Sing, G. Berner, K. Goss, A. Müller, A. Ruff, A. Wetscherek, S. Thiel, J. Mannhart, S. A. Pauli, C. W. Schneider, P. R. Willmott, M. Gorgoi, F. Schaefers, and R. Claessen, Phys. Rev. Lett. **102**, 176805 (2009).

[32] J. Fujii, B. R. Salles, M. Sperl, S. Ueda, M. Kobata, K. Kobayashi, Y. Yamashita, P. Torelli, M. Utz, C. S. Fadley, A. X. Gray, J. Braun, H. Ebert, I. Di Marco, O. Eriksson, P. Thunström, G. H. Fecher, H. Stryhanyuk, E. Ikenaga, J. Minár, C. H. Back, G. van der Laan, and G. Panaccione, Phys. Rev. Lett. **111**, 097201 (2013).

[33] P. Sadhukhan, S. W. D′Souza, V. K. Singh, R. S. Dhaka, A. Gloskovskii, S. K. Dhar, P. Raychaudhuri, A. Chainani, A. Chakrabarti, and S. R. Barman, Phys. Rev. B **99**, 035102 (2019).

[34] Hard X-ray Photoelectron Spectroscopy (HAXPES), edited by J. Woicik (Springer International, Switzerland, 2016).

[35] S. Sarkar, M. Krajčí, P. Sadhukhan, V. K. Singh, A. Gloskovskii, P. Mandal, V. Fournèe, M.-C. de Weerd, J. Ledieu, I. R. Fisher, and S. R. Barman, Phys. Rev. B **103**, L241106 (2021).

[36] M. Matsunami, M. Oura, K. Tamasaku, T. Ishikawa, S. Ideta, K. Tanaka, T. Takeuchi, T. Yamada, A. P. Tsai, K. Imura, K. Deguchi, N. K. Sato, and T. Ishimasa, Phys. Rev. B **96**, 241102(R) (2017).

[37] J. Nayak, M. Maniraj, A. Gloskovskii, M. Krajčí, S. Sebastian, I. R. Fisher, K. Horn, and S. R. Barman, Phys. Rev. B **91**, 235116 (2015).

[38] S. Sarkar, P. Sadhukhan, V. K. Singh, A. Gloskovskii, K. Deguchi, N. Fujita, and S. R. Barman, Phys. Rev. Res. **3**, 013151 (2021).

[39] S. Tanuma, C. J. Powell, and D. R. Penn, Surf. Intf. Anal. **43**, 689 (2011); C. J. Powell, A. Jablonski, I. S. Tilinin, S. Tanuma, and D. R. Penn, J. Electron Spectros. Relat. Phenom. **98-99**, 1 (1999).

[40] D.T.L. van Agterveld and G. Palasantzas, Appl. Surf. Sci. **152**, 250 (1999).

[41] J. Strempfer, S. Francoual, D. Reuther, D. K. Shukla, A. Skaugen, H. Schulte-Schrepping, T. Kracht, and H. Franz, J. Sync. Rad. **20**, 541 (2013).

[42] A. Gloskovskii, G. Stryganyuk, G. H. Fecher, C. Felser, S. Thiess, H. Schulz-Ritter, W. Drube, G. Berner, M. Sing, R. Claessen, and M. Yamamoto, J. Electron Spectrosc. Relat. Phenom. **185**, 47 (2012).

[43] G. Kresse and J. Furthmuller, Phys. Rev. B **54**, 11169 (1996).

[44] G. Kresse and D. Joubert, Phys. Rev. B **59**, 1758 (1999).

[45] J. P. Perdew, K. Burke, and M. Ernzerhof, Phys. Rev. Lett. **77**, 3865 (1996).

[46] J. P. Perdew, K. Burke, and M. Ernzerhof, Phys. Rev. Lett. **78**, 1396 (1997).

[47] M. Mihalkovič and M. Widom, Phys. Rev. B **75**, 014207 (2007).

[48] M. Widom and M. Mihalkovič, http://alloy.phys.cmu.edu/

[49] J. Wolny, M. Duda, and B. Kozakowski, Journal of Physics: Conference Series **226**, 012035 (2010).

[50] See Supplemental Material for Figs. S1-S5.

[51] A. Matilainen, K. Pussi, R. D. Diehl, M. Hahne, P. Gille, E. Gaudry, L. N. Serkovic Loli, G. M. McGuirk, M.-C. de Weerd, V. Fournèe, and J. Ledieu, Phys. Rev. B **92**, 014109 (2015).

[52] S. R. Barman and D. D. Sarma, Phys. Rev. B **51**, 4007 (1995).

[53] J. J. Yeh and I. Lindau, At. Data Nucl. Data Tables **32**, 1 (1985).

[54] S. Doniach and M. Šunjic, J. Phys. C **3**, 287 (1970).

[55] C. Biswas, A. K. Shukla, S. Banik, V. K. Ahire, and S. R. Barman, Phys. Rev. B **67**, 165416 (2003).

[56] C. Biswas, A. K. Shukla, S. Banik, S. R. Barman, and A. Chakrabarti, Phys. Rev. Lett. **92**, 11 (2004).

[57] C. Fadley, J. Electron Spectrosc. Relat. Phenom. **2**, 178 (2010).

[58] Y. Takata, Y. Kayanuma, M. Yabashi, K. Tamasaku, Y. Nishino, D. Miwa, Y. Harada, K. Horiba, S. Shin, S. Tanaka, E. Ikenaga, K. Kobayashi, Y. Senba, H. Ohashi, and T. Ishikawa, Phys. Rev. B 75, 233404 (2007).

[59] T. Fujikawa, H. Arai, R. Suzuki, H. Shinotsuka, L. Kover, and N. Ueno, J. Elect. Spectros. Relat. Phenom. **162**, 146 (2008).

[60] Y. Takata, Y. Kayanuma, S. Oshima, S. Tanaka, M. Yabashi, K. Tamasaku, Y. Nishino, M. Matsunami, R. Eguchi, A. Chainani, M. Oura, T. Takeuchi, Y. Senba, H. Ohashi, S. Shin, and T. Ishikawa, Phys. Rev. Lett. **101**, 137601 (2008).

[61] S. Suga, A. Sekiyama, H. Fujiwara, Y Nakatsu, T Miyamachi, S Imada, P Baltzer, S Niitaka, H Takagi, K Yoshimura, M Yabashi, K Tamasaku, A Higashiya, and T Ishikawa, New. J. Phys. 11, 073025 (2009).

[62] S. Suga, S. Itoda, A. Sekiyama, H. Fujiwara, S. Komori, S. Imada, M. Yabashi, K. Tamasaku, A. Higashiya, T. Ishikawa, M. Shang, and T. Fujikawa, Phys. Rev. B **86**, 035146 (2012).

[63] M. Maniraj, A. Rai, S. R. Barman, M. Krajčí, D. L. Schlagel, T. A. Lograsso, and K. Horn, Phys. Rev. B **90**, 115407 (2014).

[64] J. Nayak, Ph.D. thesis, Devi Ahilya University, Indore (2014); http://hdl.handle.net/10603/97405

[65] M. Mori, S. Matsuo, T. Ishimasa, T. Matsuura, K. Kamiya, H. Inokuchi, and T. Matsukawa, J. Phys.: Condens. Matter **3**, 767 (1991).

[66] J. Dolinsěk and A. Smontara, Isr. J. Chem. **51**, 1246 (2011).

[67] R. S. Dhaka and S. R. Barman, Phys. Rev. Lett. **104**, 036803 (2010).

[68] T. Grenet and M.C. Cheynet, Eur. Phys. J. B **13**, 701 (2000).

[69] M. Zurkirch, M. DeCrescenzi, M. Erbudak, and A. R. Kortan, Phys. Rev. B **56**, 16 (1997).

[70] S. R. Barman, C. Biswas, and K. Horn, Phys. Rev. B **69**, 045413 (2004).

[71] P. Sadhukhan, D. Pandey, V. K. Singh, S. Sarkar, A. Rai, K. Bhattacharya, A. Chakrabarti, and S. R. Barman, Appl. Surf. Sci. **506**, 144606 (2020).

[72] P. Sadhukhan, S. Barman, T. Roy, V. K. Singh, S. Sarkar, A. Chakrabarti, and S. R. Barman, Phys. Rev. B **100**, 235404 (2019).

[73] P. Scheid, C. Chatelier, J. Ledieu, V. Fournèe, and E. Gaudry, Acta Cryst. **A75**, 314 (2019).

[74] J. Grin, U. Burkhardt, M. Ellner, and K. Peters, Z. Kristallogr. Krist. **209**, 479 (1993).